ACS APPLIED ELECTRONIC MATERIALS

pubs.acs.org/acsaelm

Article

Wafer-Scale Graphene Field-Effect Transistor Biosensor Arrays with Monolithic CMOS Readout

Miika Soikkeli,* Anton Murros, Arto Rantala, Oihana Txoperena, Olli-Pekka Kilpi, Markku Kainlauri, Kuura Sovanto, Arantxa Maestre, Alba Centeno, Kari Tukkiniemi, David Gomes Martins, Amaia Zurutuza, Sanna Arpiainen, and Mika Prunnila

Cite This: *ACS Appl. Electron. Mater.* 2023, 5, 4925−4932

Read Online

ACCESS | Metrics & More | Article Recommendations | Supporting Information

ABSTRACT: The reliability of analysis is becoming increasingly important as point-of-care diagnostics are transitioning from single-analyte detection toward multiplexed multianalyte detection. Multianalyte detection benefits greatly from complementary metal-oxide semiconductor (CMOS) integrated sensing solutions, offering miniaturized multiplexed sensing arrays with integrated readout electronics and extremely large sensor counts. The development of CMOS back end of line integration compatible graphene field-effect transistor (GFET)-based biosensing has been rapid during the past few years, in terms of both the fabrication scale-up and functionalization toward biorecognition from real sample matrices. The next steps in industrialization relate to improving reliability and require increased statistics. Regarding functionalization toward truly quantitative sensors, on-chip bioassays with improved statistics require sensor arrays with reduced variability in functionalization. Such multiplexed bioassays, whether based on graphene or on other sensitive nanomaterials, are among the most promising technologies for label-free electrical biosensing. As an important step toward that, we report wafer-scale fabrication of CMOS-integrated GFET arrays with high yield and uniformity, designed especially for biosensing applications. We demonstrate the operation of the sensing platform array with 512 GFETs in simultaneous detection for the sodium chloride concentration series. This platform offers a truly statistical approach on GFET-based biosensing and further to quantitative and multianalyte sensing. The reported techniques can also be applied to other fields relying on functionalized GFETs, such as gas or chemical sensing or infrared imaging.

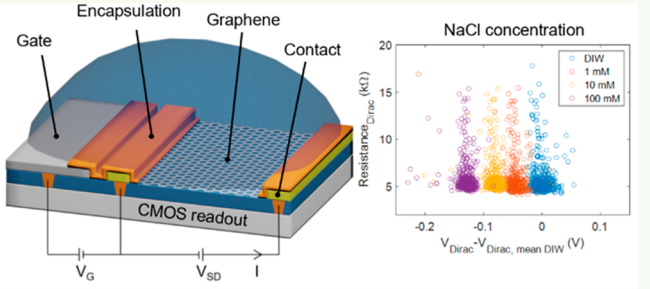

KEYWORDS: *graphene, CMOS, monolithic, integration, wafer-scale, field-effect transistor, biosensor, statistics*

1. INTRODUCTION

Point-of-care (PoC) diagnostics is transitioning from single-analyte detection toward multiplexed multianalyte detection, which increases the importance of reliable statistical analysis.[1] When targeting quantitative or multianalyte sensors, simultaneous screening of a sample for several different analytes is required together with adequate statistics to be able to exclude individual false signal sources. Traditionally multiplexed testing is done on enzyme-linked immunosorbent assays (ELISA),[2] where every analyte and receptor pair is measured individually. More advanced multiplexed multianalyte diagnostic solutions can be achieved on a single chip by using sensor arrays with integrated complementary metal-oxide semiconductor (CMOS) readout. The benefits of CMOS integration include low cost, dense array formation, lower power consumption, label-free detection mechanism, readout integration, and smaller device dimensions[3,4] which all are very beneficial especially for PoC applications.

One of the most promising label-free biosensing technologies, compatible with CMOS integration, is sensitive and selective graphene field-effect transistor (GFET) sensors based on chemical vapor deposited (CVD) graphene. The use of GFETs has been demonstrated for peptides and antibodies,[5] attomolar-level DNA hybridization,[6] zika-virus detection,[7] and recently also for COVID-19 causative virus monitoring.[8,9] With CMOS-integrated GFET arrays, it is possible to overcome the common problems in field-effect biosensing related to the limited detection ranges in real-life sample matrices by utilizing PEG-polymer-aided functionalization schemes.[9,10] This is all very promising considering the prospects of GFETs in label-free electrical sensing for early

Received: May 26, 2023
Accepted: August 14, 2023
Published: August 24, 2023

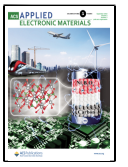

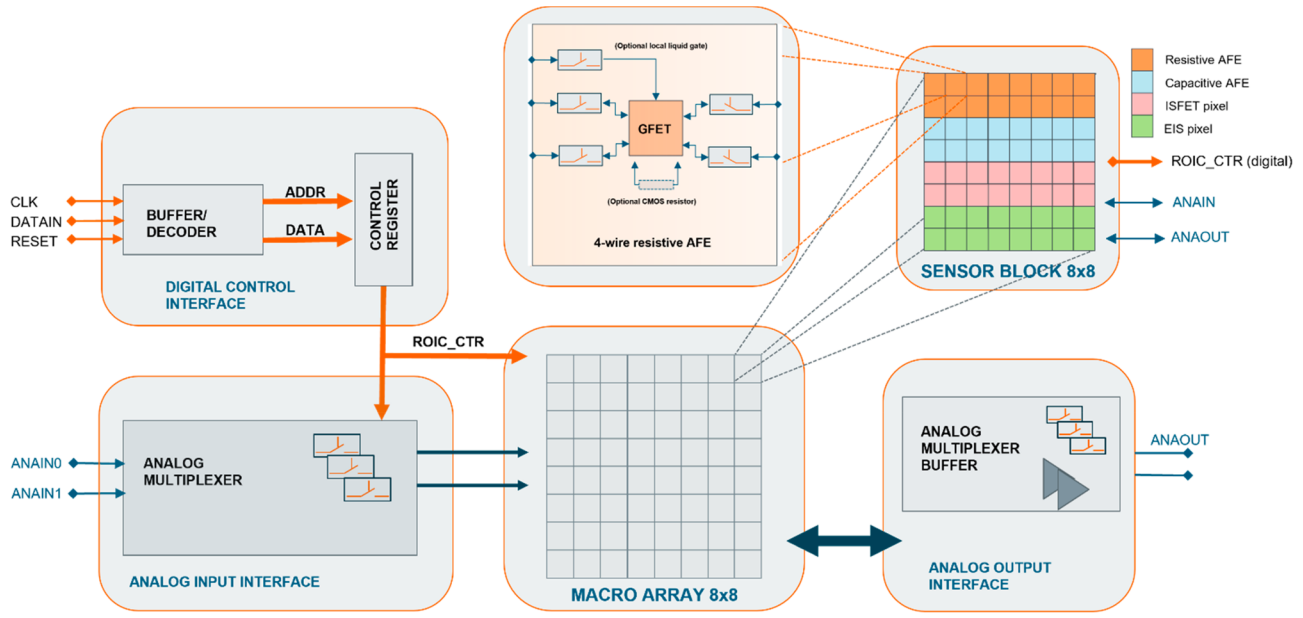

Figure 1. Block diagram of the CMOS system with a single large read-out matrix having common global level control and output signal processing units. Different read-out electronics have been laid out around the matrix area to obtain uniform coverage for each sensor type. The different sensor read-out circuits are grouped into an 8 × 8 submatrix. In the whole ASIC there is a macroarray consisting of 8 × 8 subarrays. Each sensor can be individually selected. Inside each subarray there are two rows of GFET sensors, capacitive graphene sensors, n- and p-type ISFET sensors, and EIS sensors. The global digital control can be used for the resistive AFE of the GFETs to select a plurality of GFETs by enabling pixel-level local CMOS switches. There is an option to select either two-wire or four-wire connection to enable a Kelvin-type resistance measurement. A local gate electrode is also possible to connect to provide a bias for the back or top gate electrode depending on process selection.

diagnostics and PoC applications requiring sensitive and specific biorecognition from biological sample matrices.

Other promising, compatible with CMOS back end of line (BEOL) integration, FET-based technologies for biosensing are based on carbon nanotube (CNT),[11] organic semiconductor,[12] and semiconductor silicon nanowire (SiNW)FET sensors.[13] All of these technologies still have some limitations that need to be addressed to get the full potential out. Organic FETs have lower charge sensitivity and dynamic range when compared to GFETs and SiNWFETs due to larger channel dimensions.[14] SiNWFETs suffer from high device-to-device variations and low carrier mobility.[15] CNTFETs have low current output, small active areas, and heterogeneous semiconductor and metal mixtures.[16] These aspects can lead to a large variation between devices and low manufacturing yields for CNTFETs.[16] GFETs offer at least similar sensitivity and easier fabrication when compared with the competing technologies. This makes GFETs a very interesting and cost-effective approach for highly sensitive label-free biosensors.

Previously, scalable CMOS-integrated biosensor solutions have been reported for example with carbon nanotubes,[16] ion-selective FETs (ISFETs),[17] extended gate field-effect transistors (EGFETs),[18] and film bulk acoustic resonators (FBARs).[19] ISFETs and EGFETs are easy to manufacture on top of the CMOS with standard processes.[17,18] ISFETs also suffer typically from device stability and drift issues.[20,21] EGFETs were originally proposed as a solution to solve the drift and stability issues of ISFETs, and the sensitivity of the devices can be improved due to the possibility for larger sensing areas.[22,23] CNT-based sensors and FBARs are harder to fabricate on CMOS readout and easily suffer from low yields in fabrication.[16,19] With CNT-based sensors, the as-grown angle of CNTs is difficult to control without deliberate alignment, and deposited films show high variability in contact resistance.[24] FBARs suffer from low yields due to residual stresses in the suspended membrane and piezoelectric layer and lengthy etching processes.[25] The possibility to integrate CVD graphene with CMOS readout on chip scale has been demonstrated earlier for broadband image detectors[26] and gas sensing.[27] The possibilities of graphene integration into CMOS BEOL have been discussed by Neumaier et al.[28] However, full BEOL integration of the graphene-based biosensor arrays has not been realized due to the lack of wafer-scale CMOS readout integration.

In this work, we demonstrate for the first-time wafer-scale CMOS integration of graphene FETs for biosensing. Functionality of the integrated GFETs for biosensing is demonstrated using simultaneous measurement of 512 GFETs for a series of sodium chloride concentration measurement. In our approach, we integrate GFETs on a CMOS multiplexer platform that enables the simultaneous measurement of hundreds of GFETs. The work done here further enables a statistical approach for multianalyte biosensing since the reliable detection of a certain analyte requires several devices and statistics for the analysis.

2. MATERIALS AND METHODS

CMOS Read-Out Design. The CMOS wafers used for GFET integration were manufactured using a standard commercial technology provided by XFAB. The 200 mm CMOS wafers utilize a 0.35 μm analogue CMOS process node with up to four metallization layers. The CMOS technology includes a wide range of active devices and high-performance analog devices.

The CMOS read-out platform was designed to support several types of postprocessed sensors. The architecture of the CMOS system and the local readout for a resistive GFET are illustrated in Figure 1. The application-specific integrated circuit (ASIC) is comprised of a macroarray consisting of 64 sensor blocks. Each sensor block is further comprised of a subarray with 64 individual sensors with four

https://doi.org/10.1021/acsaelm.3c00706
ACS Appl. Electron. Mater. 2023, 5, 4925−4932

different read-out schemes. Each macroarray thus contains readouts for up to 4096 individual devices. Here we focus only on the devices with analog front end (AFE) designed for the resistive read-out of the GFETs.

The global digital control is used to select the GFETs by enabling pixel-level local CMOS switches. For each GFET there is an option to select either two-wire or four-wire connection to enable a Kelvin-type resistance measurement. The global control of the resistive GFETs operates as follows. The digital control SPI interface is utilized to fetch a code string to address the GFET(s) to be analyzed. The address decoder selects the corresponding GFET(s) and enables analogue switches and the output multiplexer. The multiplexer output is in the case of the GFET read-out fed directly to ASIC pads. In this ASIC design, the GFET resistance is measured using external laboratory equipment. CMOS readout also enables the integration of the resistance meter functionality on the chip level, which will be evaluated in future designs to increase the functionality of the system.

CMOS Postprocessing of the Graphene Field-Effect Transistors. The postprocessed sensors were designed to utilize half of the available readouts to allow space for local liquid gate electrodes and in addition to an on-chip global liquid gate electrode. These liquid gate electrodes can gate the graphene channels in biosensing measurements. The global platinum liquid gate electrode is formed of 64 stripes that are 12 μm wide and 6400 μm long. The usage of similar pseudoreference electrodes has been demonstrated to work reliably for GFETs.[29] The selected options result in 512 individual GFETs being fabricated for each chip. A microscope image of the fabricated GFET sensors is shown in Figure 2a.

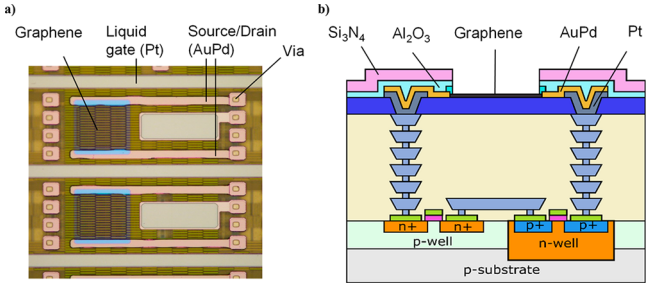

Figure 2. (a) Graphene FETs on top of the CMOS readout circuit connected to the vias on the right side. The vias on the left side are not connected, leaving more space for local and global liquid gate options. (b) Schematic illustration of the postprocessed GFET on CMOS readout. Pt was used to fill the vias and to form a liquid gate mesh on the surface of the chips. Contacts between graphene and the vias have been formed with AuPd metals. Graphene has been patterned by using an Al_2O_3 protective layer. The device has been passivated with Al_2O_3 and Si_3N_4 layers, leaving only the graphene channel and liquid gate electrode surfaces open for the liquid measurements.

A schematic illustration of the postprocessed GFET on the CMOS readout is presented in Figure 2b. Wafer-scale postprocessing was started by filling the CMOS vias by Pt deposited by sputtering and patterned using a lift-off process. All postprocess patterning steps were done by standard UV lithography. In addition to the via contacts, the Pt metal layer also defined the on-chip Pt liquid gate that is used to gate the graphene channel. In the next step, CVD graphene was transferred onto the CMOS wafer by using a wet transfer method. After the graphene transfer, the wafer was annealed for 16 h at 300 °C in a vacuum. A 50-nm-thick AuPd alloy contact metal was deposited by evaporation and lift-off. Next the graphene surface was protected with a 50-nm-thick Al_2O_3 grown by atomic layer deposition (ALD). ALD growth on graphene was seeded using an evaporated 1-nm-thick Al film oxidized in the evaporation chamber.

Graphene patterning was done by wet etching the protective Al_2O_3 in H_3PO_4 followed by etching the graphene in an O_2 plasma. After the graphene patterning, the devices were passivated by 50-nm-thick ALD Al_2O_3 and 120-nm-thick plasma-enhanced chemical vapor deposition (PECVD) Si_3N_4. Finally, the passivation of the devices was opened from the top of the graphene channels by dry etching of Si_3N_4 and wet etching the Al_2O_3. The success of the channel opening step was evaluated by an etch step and surface characterization of the graphene channels by atomic force microscopy (AFM) (Figure SI1). The graphene quality at the end of the processing was also characterized by Raman spectroscopy (Figure SI3). The wafers were then diced into single CMOS microsystem chips.

Graphene FET Measurements. For the characterization, five sensor chips were selected across the diced wafer. The chips were wire bonded onto chip carriers for electrical measurements. A detector chip wire bonded on a chip carrier is shown in Figure 3a. For one of

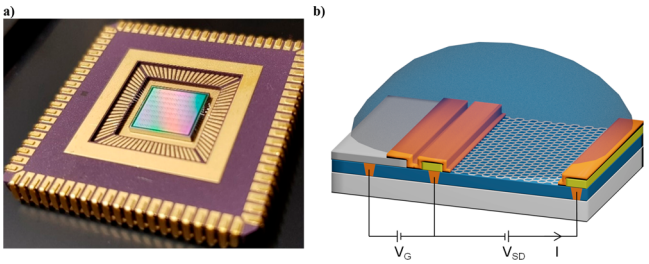

Figure 3. (a) A chip with CMOS-integrated GFETs wire bonded on a chip carrier. (b) Electrical measurement configuration of the GFETs. The on-chip platinum liquid gate electrode is used to control the liquid gate voltage (V_G). The current (I) in the graphene channel is measured between the source and drain electrodes with a 0.1 V source−drain bias (V_{SD}) over the channel.

the chips, the bonded wires were protected with a polydimethylsiloxane (PDMS) coating to enable a measurement in liquid. Electrical measurement configuration for the GFETs is shown in Figure 3b. A parameter analyzer is used together with the CMOS multiplexer on the chips for the measurement and biasing of the devices. Liquid gate voltage (V_G) is controlled by using the global on-chip Pt liquid gate. The current (I) in the graphene channel is measured with a 0.1 V source−drain bias (V_{SD}) over the channel.

The graphene detector surface was cleaned with isopropanol and deionized water (DIW), before characterization of the devices in DIW and in a series of sodium chloride (NaCl) with different concentrations. The measurement in DIW was repeated once before and after the actual measurement series to ensure that the devices are stable. For DIW and each concentration of NaCl, the sensor surface was further washed five times with a 100 μL droplet of the corresponding solution to ensure that the concentration on top of the chip was correct.

To evaluate the response of the sensor chip to the physiological solutions, the ionic strength of the sample solution was varied. The tests included measurements in DIW and 1, 10, and 100 mM NaCl solutions. The channel of the graphene FETs is charged, and an electrical double layer (EDL) is formed on the graphene−liquid interface to neutralize the charged surface. The thickness of the EDL can be estimated by using the Debye length, which corresponds to the distance at which the electric potential has decreased in magnitude by $1/e$. It can be calculated for the monovalent electrolytes at room temperature according to the following equation:

$$\lambda_D = 0.304/\sqrt{I}$$

where I is the ionic strength of the solution.

Based on the formula, the Debye lengths for the 1, 10, and 100 mM NaCl concentrations are 9.6 3.0, and 0.96 nm, respectively. The Debye length corresponds approximately to the gate oxide thickness of the GFETs. The dielectric constant of the DIW is 78.4[30,31] at 25 °C, and approximately the same value applies for the low NaCl concentration solutions.[32]

https://doi.org/10.1021/acsaelm.3c00706
ACS Appl. Electron. Mater. 2023, 5, 4925−4932

3. RESULTS AND DISCUSSION

Graphene FET Yield and Uniformity. In this work, we focused on studying 512 GFETs with a resistive readout option from the five selected chips numbered from #1 to #5. The resistance values measured in ambient conditions without gating from chip #4 are shown in Figure 4a, and histograms of the measured resistance values for 5 chips are in Figure 4b. The average resistance values and standard deviations (SD) are 790 Ω (SD = 120 Ω), 830 Ω (SD = 140 Ω), 810 Ω (SD = 120 Ω), 770 Ω (SD = 100 Ω). and 810 Ω (SD = 160 Ω) for chips #1−5, respectively. This demonstrates good process stability over the whole wafer. A single noncontacted GFET was subtracted from the data for chips #3 and #5. This gives us an extremely high device yield of 99.9% with 2558 devices working out of the 2560 measured devices.

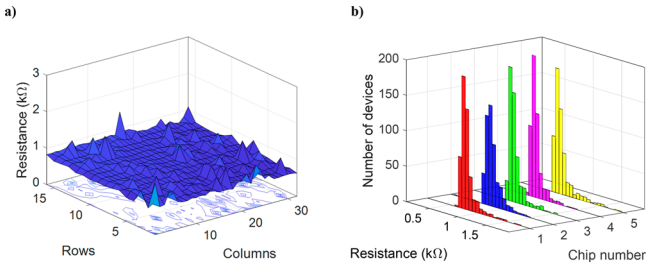

Figure 4. (a) Resistance values of the 512 GFETs measured from chip 4. The average resistance is 770 Ω (SD = 100 Ω). (b) Histograms of the resistances measured from the five chips. The average resistance values are 790 Ω (SD = 120 Ω), 830 Ω (SD = 140 Ω), 810 Ω (SD = 120 Ω), 770 Ω (SD = 100 Ω), and 810 Ω (SD = 160 Ω) for chips #1−5, respectively. A single noncontacted GFET was subtracted from the data for chips #3 and #5. This gives us a very high device yield of 99.9% with 2558 devices working out of the 2560 measured devices.

Characterization in Deionized Water. The performance and stability of the GFETs was first evaluated by electrical measurements in DIW. The GFETs were characterized twice in DIW to obtain resistance of the devices as a function of the gate voltage. The V_G was applied using an on-chip Pt electrode to all the GFETs. The results are shown in Figures 5a and SI2. The data have been normalized to the average Dirac peak voltage value of 1.45 V (SD = 0.01 V) measured in DIW. A histogram of the normalized Dirac peak voltage values is shown in Figure 5b. The average Dirac peak resistance is 6 kΩ (SD = 2 kΩ). The variation for the Dirac peak voltage is low, but some of the devices show higher resistance levels, which is most likely caused either by a poor contact between the metal and graphene or by possible defects in the graphene layer. Few devices also show a higher deviation in the Dirac peak voltage, which can possibly be caused by resist or passivation layer residues on top of the graphene channel. These residues are left from processing and cause additional doping and a change in the effective gate capacitance. Another possible reason for this is the use of DIW as a dielectric, as it is possible that there are small air bubbles on the surface of some of the GFETs that interfere with the gating.

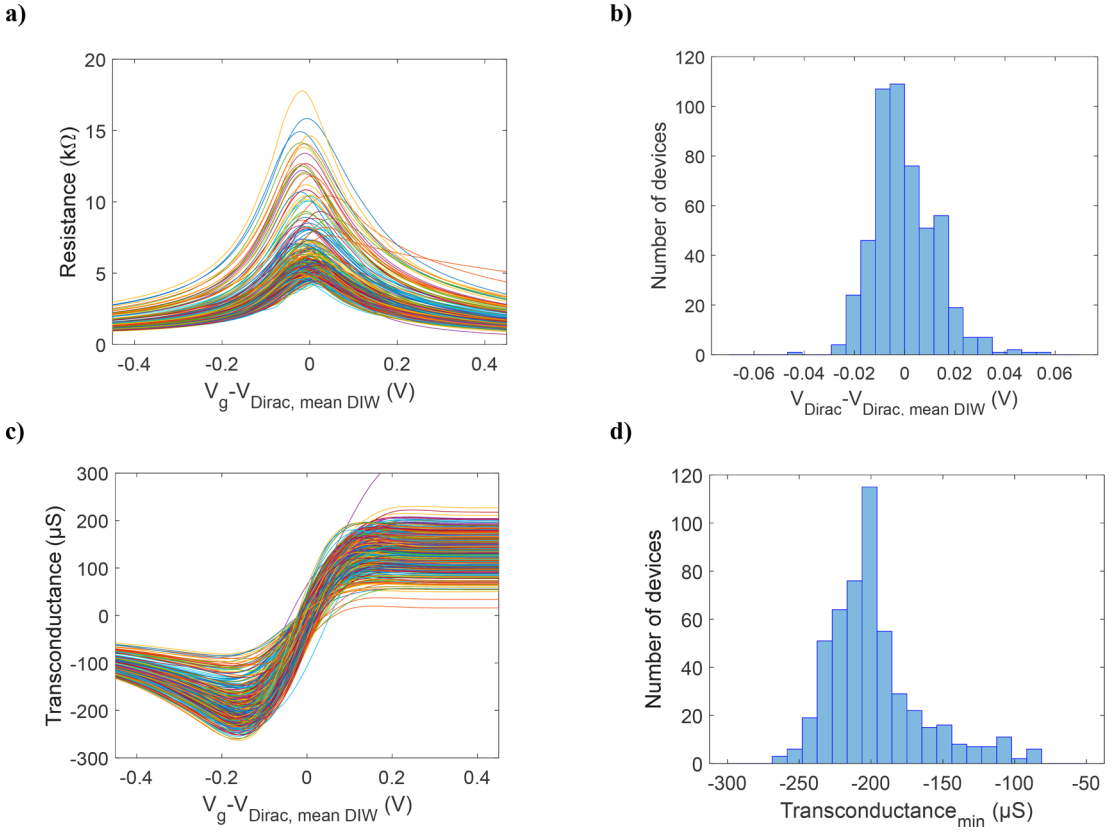

Figure 5. (a) Resistance values as a function of the $V_g - V_{Dirac,mean\ DIW}$ for the 512 GFETs in DIW. (b) Histogram of $V_{Dirac} - V_{Dirac,mean\ DIW}$ for the 512 GFETs in DIW. (c) Transconductance values as a function of the $V_g - V_{Dirac,mean\ DIW}$ for the 512 GFETs. (d) Histogram of the minimum transconductance values for the 512 GFETs.

https://doi.org/10.1021/acsaelm.3c00706
ACS Appl. Electron. Mater. 2023, 5, 4925−4932

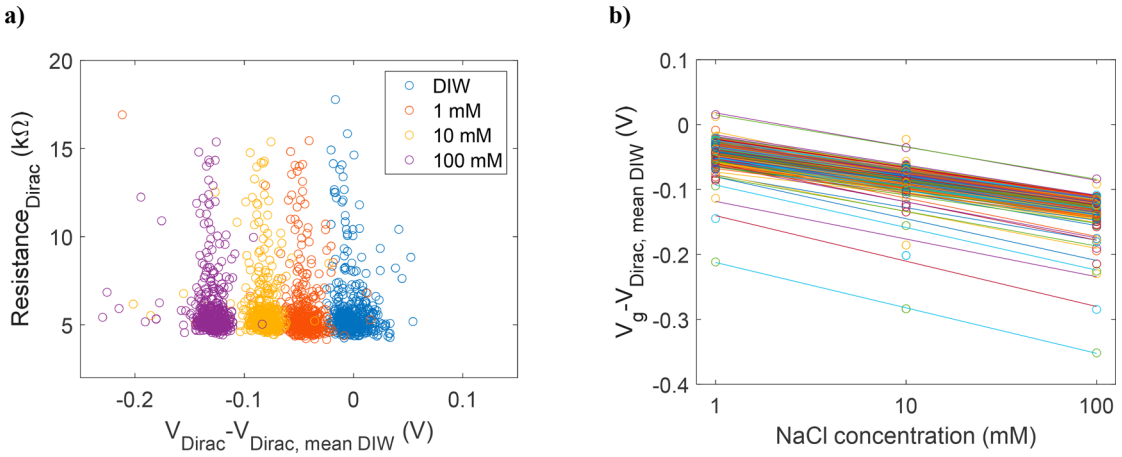

Figure 6. (a) Resistance values at V_{Dirac} as a function of $V_{Dirac}-V_{Dirac, mean DIW}$ for the 512 GFETs in deionized water and 1, 10, and 100 mM sodium chloride solutions. (b) $V_{Dirac}-V_{Dirac, mean DIW}$ values as a function of NaCl concentration for the 512 GFETs used to extract the sensitivity of the devices in the 1 to 100 mM concentration range. The obtained average sensitivity of the GFETs for the NaCl solution in the 1 to 100 mM concentration range is 42 mV/dec (SD = 4 mV/dec).

The transconductance (g_m) of the GFETs is defined as the derivative of the channel current, with respect to V_G. The transconductances as a function of the gate voltage are shown in Figure 5c. The transconductance maximum and minimum (Figure 5d) are 140 μS (SD = 33 μS) and −198 μS (SD = 33 μS), respectively. The corresponding voltage values for the maximum and minimum transconductance values are 180 mV (SD = 30 mV) and −160 mV (SD = 15 mV), respectively. The transconductance can be used to estimate the sensitivity of the devices in the biodetection. The attachment of the biomolecules typically induces gating to the graphene channel, which causes the Dirac peak to shift. This shift can be measured as a change in the current versus time when measuring with a set gate voltage. The higher transconductance of the device then leads to a higher response in the measured current.

Characterization in Sodium Chloride Solutions. Similarly to the characterization in DIW, the GFETs were characterized to obtain resistance and transconductance values of the devices as a function of the gate voltage for each NaCl concentration (Figure SI3 and Table SI1). The measured resistance and transconductance values indicate that the main response is the shift of the Dirac peak position. The behavior can be explained with a doping change in the graphene channel caused by the change in the gate capacitance.[33,34] After the NaCl concentration series, an additional measurement was done in DIW to ensure that the devices return to the baseline established in the DIW characterization (Figure SI2).

The extracted transconductance values can be used to estimate the mobility of the devices by using the following equation:

$$\mu = g_m \frac{L}{W} \frac{1}{C_{TOT} V_{SD}} \quad (1)$$

where L is the length and W is the width of the graphene FET channel, V_{SD} is the source−drain voltage, and the C_{TOT} is the total capacitance. C_{TOT} can be estimated according to the following equation:

$$\frac{1}{C_{TOT}} = \frac{1}{C_{Pt}} + \frac{1}{C_G} + \frac{1}{C_Q} \quad (2)$$

where C_{Pt} is the double-layer capacitance at the platinum reference electrode, C_G is the double-layer capacitance at the graphene electrode, and the C_Q is the quantum capacitance of the graphene. When the size of the platinum electrode is much larger than the size of the graphene electrode ($A_{Pt} > 1900 \times A_G$), the effect on the total capacitance is negligible, and only the quantum capacitance and the double-layer capacitance at the graphene electrode need to be considered. The experimental value of quantum capacitance is reported to be between 2 and 11 μF cm^{-2}, which depends on the gate potential and charged impurities.[35] With a moderate charge impurity level (0.5×10^{12} cm^{-2}) and graphene potential (±0.2 V) corresponding to the maximum and minimum transconductance point values, the quantum capacitance is estimated to be around 4 μF cm^{-2}. The double-layer capacitance at the graphene electrode can be calculated by using the following equation:

$$C_G = \frac{\varepsilon_0 \varepsilon_r}{\lambda_D} \quad (3)$$

where ε_0 is the permittivity of free space and ε_r is the dielectric constant. By substituting eqs 2 and 3 with eq 1 we can extract the average mobility values in 1 mM NaCl by using the measured transconductance values. The mobility values are 1030 cm^2/(V s) (SD = 170 cm^2/(V s)) and 900 cm^2/(V s) (SD = 190 cm^2/(V s)) for holes and electrons, respectively.

The resistance values at the Dirac peak and the corresponding Dirac peak voltage values for DIW and each NaCl concentration are shown in Figure 6a. The Dirac peak voltage that has been normalized to the average value in DIW changes from 0 mV (SD = 13 mV) in DIW to 45 mV (SD = 15 mV), 82 mV (SD = 15 mV), and 129 mV (SD = 18 mV) for 1, 10, and 100 mM NaCl concentrations, respectively. The data show that the average resistance value at the Dirac peak stays stable at 6 kΩ (SD = 2 kΩ) when the concentration is changed, and the main signal is the shift of the Dirac peak voltage position. This indicates that the dominating sensing mechanism is electrostatic gating of the GFETs.[36] The sensitivity of each individual device has been estimated by using the measured Dirac voltage values and linear fitting, as shown in Figure 6b. The obtained average sensitivity of the

https://doi.org/10.1021/acsaelm.3c00706
ACS Appl. Electron. Mater. 2023, 5, 4925−4932

GFETs for the NaCl concentrations in the 1 to 100 mM range is 42 mV/dec (SD = 4 mV/dec).

4. CONCLUSIONS

We demonstrate, for the first-time, wafer-scale GFET CMOS integration for biosensing with a device yield higher than 99% with a low device-to-device variability. We believe this approach will be crucial when commercializing GFET-based biosensors, enabling multianalyte sensing and the statistical analysis required for biologically quantitative on-chip bioassays. In the future, on-chip multianalyte sensing could enable efficient screening of multiple viruses with sufficient statistics for reliable detection from a single small analyte sample. The platform could be combined for example with the functionalization approach shown by Silvestri et al. on similar non-CMOS integration GFETs[8] to take the next steps toward multianalyte viral sensing. This technology enables the use of different sizes of GFET channels, with the possible number of GFETs ranging from thousands to millions of devices depending on the ASIC circuit design and technology. This flexibility in the number of and size of the devices allows for a wider set of applications where large amounts of biological information need to be evaluated, such as gene sequencing.[37,38]

In addition to its application in quantitative bioassays, CMOS multiplexing can also be a valuable tool in the assay development phase. The most common issues in the development of FET-based biosensing are related to the reliability and repeatability of individual devices and analysis. In many cases, the sensor chips are only used in a single measurement; hence, individual faulty devices, voids in the functionalization, and small air bubbles can lead to misinterpretation of results. The large-scale statistics provided by CMOS multiplexed sensor arrays on a single chip will improve the general reliability of the analysis and enable easy removal of defective devices from the data.

The other benefits that the monolithic integration of GFETs offers are reduction in environmental noise and simplified connections, when compared to hybrid off-chip sensors.[39] Furthermore, multiplexing sensor arrays offer advantages in sensor defect exclusion and wider dynamic ranges by allowing for varying sensor design for different sensitivities.[37] The demonstrated technology also opens possibilities for the wafer-scale fabrication of CMOS-integrated GFET-based gas sensor arrays[27] and infrared cameras[26] that have been demonstrated in the past. In this sense, the development of GFETs as a generic template that can be made specific by the choice of functionalization allows for the adoption of this technology in a wide range of different applications.[40] With CMOS integration, the readout can be tailored to fit specific needs, which leads to a versatile sensor platform.

■ ASSOCIATED CONTENT

Supporting Information

The Supporting Information is available free of charge at https://pubs.acs.org/doi/10.1021/acsaelm.3c00706.

Surface characterization with AFM, sensor array stability measurements, and additional data for the measurements in different sodium chloride concentrations (PDF)

■ AUTHOR INFORMATION

Corresponding Author

Miika Soikkeli − *VTT Technical Research Centre of Finland Ltd, FI-02044 VTT Espoo, Finland;* orcid.org/0000-0002-8014-7875; Email: miika.soikkeli@vtt.fi

Authors

Anton Murros − *VTT Technical Research Centre of Finland Ltd, FI-02044 VTT Espoo, Finland*

Arto Rantala − *VTT Technical Research Centre of Finland Ltd, FI-02044 VTT Espoo, Finland*

Oihana Txoperena − *Graphenea Semiconductor SLU, 20009 San Sebastian, Spain*

Olli-Pekka Kilpi − *VTT Technical Research Centre of Finland Ltd, FI-02044 VTT Espoo, Finland*

Markku Kainlauri − *VTT Technical Research Centre of Finland Ltd, FI-02044 VTT Espoo, Finland*

Kuura Sovanto − *VTT Technical Research Centre of Finland Ltd, FI-02044 VTT Espoo, Finland*

Arantxa Maestre − *Graphenea Semiconductor SLU, 20009 San Sebastian, Spain*

Alba Centeno − *Graphenea Semiconductor SLU, 20009 San Sebastian, Spain*

Kari Tukkiniemi − *VTT Technical Research Centre of Finland Ltd, FI-02044 VTT Espoo, Finland*

David Gomes Martins − *VTT Technical Research Centre of Finland Ltd, FI-02044 VTT Espoo, Finland*

Amaia Zurutuza − *Graphenea Semiconductor SLU, 20009 San Sebastian, Spain*

Sanna Arpiainen − *VTT Technical Research Centre of Finland Ltd, FI-02044 VTT Espoo, Finland*

Mika Prunnila − *VTT Technical Research Centre of Finland Ltd, FI-02044 VTT Espoo, Finland*

Complete contact information is available at: https://pubs.acs.org/10.1021/acsaelm.3c00706

Author Contributions

The manuscript was written through contributions of all authors.

Notes

The authors declare no competing financial interest.

■ ACKNOWLEDGMENTS

The authors acknowledge the support by the European Union's Horizon 2020 research and innovation program under the grant agreements Graphene Flagship (881603) and 2D-EPL (952792) and the Academy of Finland (grant 342586) and Business Finland through co-innovation project DigiDNA (grant 1869/31/2016).

■ REFERENCES

(1) Kim, H.; Huh, H. J.; Park, E.; Chung, D.-R.; Kang, M. Multiplex Molecular Point-of-Care Test for Syndromic Infectious Diseases. *Biochip J.* **2021**, *15* (1), 14−22.

(2) Engvall, E.; Jonsson, K.; Perlmann, P. Enzyme-Linked Immunosorbent Assay. II. Quantitative Assay of Protein Antigen, Immunoglobulin g, by Means of Enzyme-Labelled Antigen and Antibody-Coated Tubes. *Biochimica et Biophysica Acta (BBA) - Protein Structure* **1971**, *251* (3), 427−434.

(3) Milgrew, M. J.; Hammond, P. A.; Cumming, D. R. S. The Development of Scalable Sensor Arrays Using Standard CMOS Technology. *Sens Actuators B Chem.* **2004**, *103* (1−2), 37−42.

(4) Bustillo, J.; Fife, K.; Merriman, B.; Rothberg, J. Development of the Ion Torrent CMOS Chip for DNA Sequencing. In *2013 IEEE International Electron Devices Meeting*; IEEE, 2013; pp 8.1.1−8.1.4, DOI: 10.1109/IEDM.2013.6724584.
(5) Soikkeli, M.; Kurppa, K.; Kainlauri, M.; Arpiainen, S.; Paananen, A.; Gunnarsson, D.; Joensuu, J. J.; Laaksonen, P.; Prunnila, M.; Linder, M. B.; Ahopelto, J. Graphene Biosensor Programming with Genetically Engineered Fusion Protein Monolayers. *ACS Appl. Mater. Interfaces* **2016**, *8* (12), 8257−8264.
(6) Campos, R.; Borme, J.; Guerreiro, J. R.; Machado, G.; Cerqueira, M. F.; Petrovykh, D. Y.; Alpuim, P. Attomolar Label-Free Detection of DNA Hybridization with Electrolyte-Gated Graphene Field-Effect Transistors. *ACS Sens* **2019**, *4* (2), 286−293.
(7) Afsahi, S.; Lerner, M. B.; Goldstein, J. M.; Lee, J.; Tang, X.; Bagarozzi, D. A.; Pan, D.; Locascio, L.; Walker, A.; Barron, F.; Goldsmith, B. R. Novel Graphene-Based Biosensor for Early Detection of Zika Virus Infection. *Biosens Bioelectron* **2018**, *100*, 85−88.
(8) Silvestri, A.; Zayas-Arrabal, J.; Vera-Hidalgo, M.; Di Silvio, D.; Wetzl, C.; Martinez-Moro, M.; Zurutuza, A.; Torres, E.; Centeno, A.; Maestre, A.; Gómez, J. M.; Arrastua, M.; Elicegui, M.; Ontoso, N.; Prato, M.; Coluzza, I.; Criado, A. Ultrasensitive Detection of SARS-CoV-2 Spike Protein by Graphene Field-Effect Transistors. *Nanoscale* **2023**, *15* (3), 1076−1085.
(9) Seo, G.; Lee, G.; Kim, M. J.; Baek, S.-H.; Choi, M.; Ku, K. B.; Lee, C.-S.; Jun, S.; Park, D.; Kim, H. G.; Kim, S.-J.; Lee, J.-O.; Kim, B. T.; Park, E. C.; Kim, S. Il. Rapid Detection of COVID-19 Causative Virus (SARS-CoV-2) in Human Nasopharyngeal Swab Specimens Using Field-Effect Transistor-Based Biosensor. *ACS Nano* **2020**, *14* (4), 5135−5142.
(10) Andoy, N. M.; Filipiak, M. S.; Vetter, D.; Gutiérrez-Sanz, Ó.; Tarasov, A. Graphene-Based Electronic Immunosensor with Femtomolar Detection Limit in Whole Serum. *Adv. Mater. Technol.* **2018**, *3* (12), No. 1800186.
(11) Jacobs, C. B.; Peairs, M. J.; Venton, B. J. Review: Carbon Nanotube Based Electrochemical Sensors for Biomolecules. *Anal. Chim. Acta* **2010**, *662* (2), 105−127.
(12) Maddalena, F.; Kuiper, M. J.; Poolman, B.; Brouwer, F.; Hummelen, J. C.; de Leeuw, D. M.; De Boer, B.; Blom, P. W. M. Organic Field-Effect Transistor-Based Biosensors Functionalized with Protein Receptors. *J. Appl. Phys.* **2010**, *108* (12), No. 124501.
(13) Chen, K.-I.; Li, B.-R.; Chen, Y.-T. Silicon Nanowire Field-Effect Transistor-Based Biosensors for Biomedical Diagnosis and Cellular Recording Investigation. *Nano Today* **2011**, *6* (2), 131−154.
(14) Syu, Y.-C.; Hsu, W.-E.; Lin, C.-T. Review—Field-Effect Transistor Biosensing: Devices and Clinical Applications. *ECS Journal of Solid State Science and Technology* **2018**, *7* (7), Q3196−Q3207.
(15) Zhang, A.; Lieber, C. M. Nano-Bioelectronics. *Chem. Rev.* **2016**, *116* (1), 215−257.
(16) Seichepine, F.; Rothe, J.; Dudina, A.; Hierlemann, A.; Frey, U. Dielectrophoresis-Assisted Integration of 1024 Carbon Nanotube Sensors into a CMOS Microsystem. *Adv. Mater.* **2017**, *29* (17), No. 1606852.
(17) Merriman, B.; R&D Team, I. T.; Rothberg, J. M. Progress in Ion Torrent Semiconductor Chip Based Sequencing. *Electrophoresis* **2012**, *33* (23), 3397−3417.
(18) Komori, H.; Niitsu, K.; Tanaka, J.; Ishige, Y.; Kamahori, M.; Nakazato, K. An Extended-Gate CMOS Sensor Array with Enzyme-Immobilized Microbeads for Redox-Potential Glucose Detection. In *2014 IEEE Biomedical Circuits and Systems Conference (BioCAS) Proceedings*; IEEE, 2014; pp 464−467, DOI: 10.1109/BioCAS.2014.6981763.
(19) Nirschl, M.; Rantala, A.; Tukkiniemi, K.; Auer, S.; Hellgren, A.-C.; Pitzer, D.; Schreiter, M.; Vikholm-Lundin, I. CMOS-Integrated Film Bulk Acoustic Resonators for Label-Free Biosensing. *Sensors* **2010**, *10* (5), 4180−4193.
(20) Chiang, J.-L.; Jan, S.-S.; Chou, J.-C.; Chen, Y.-C. Study on the Temperature Effect, Hysteresis and Drift of PH-ISFET Devices Based on Amorphous Tungsten Oxide. *Sens Actuators B Chem.* **2001**, *76* (1−3), 624−628.
(21) Miscourides, N.; Georgiou, P. ISFET Arrays in CMOS: A Head-to-Head Comparison Between Voltage and Current Mode. *IEEE Sens J.* **2019**, *19* (4), 1224−1238.
(22) van der spiegel, J.; Lauks, I.; Chan, P.; Babic, D. The Extended Gate Chemically Sensitive Field Effect Transistor as Multi-Species Microprobe. *Sens. Actuators* **1983**, *4*, 291−298.
(23) Singh, K.; Pang, S.-T.; Pan, T.-M. Amorphous ZnSnxOy Fabricated at Room-Temperature for Flexible PH-EGFET Sensor. *IEEE Trans. Electron Devices* **2021**, *68* (2), 793−797.
(24) Schroeder, V.; Savagatrup, S.; He, M.; Lin, S.; Swager, T. M. Carbon Nanotube Chemical Sensors. *Chem. Rev.* **2019**, *119* (1), 599−663.
(25) Chen, G.; Zhao, X.; Wang, X.; Jin, H.; Li, S.; Dong, S.; Flewitt, A. J.; Milne, W. I.; Luo, J. K. Film Bulk Acoustic Resonators Integrated on Arbitrary Substrates Using a Polymer Support Layer. *Sci. Rep* **2015**, *5* (1), 9510.
(26) Goossens, S.; Navickaite, G.; Monasterio, C.; Gupta, S.; Piqueras, J. J.; Pérez, R.; Burwell, G.; Nikitskiy, I.; Lasanta, T.; Galán, T.; Puma, E.; Centeno, A.; Pesquera, A.; Zurutuza, A.; Konstantatos, G.; Koppens, F. Broadband Image Sensor Array Based on Graphene−CMOS Integration. *Nat. Photonics* **2017**, *11* (6), 366−371.
(27) Mortazavi Zanjani, S. M.; Holt, M.; Sadeghi, M. M.; Rahimi, S.; Akinwande, D. 3D Integrated Monolayer Graphene−Si CMOS RF Gas Sensor Platform. *NPJ. 2D Mater. Appl.* **2017**, *1* (1), 36.
(28) Neumaier, D.; Pindl, S.; Lemme, M. C. Integrating Graphene into Semiconductor Fabrication Lines. *Nat. Mater.* **2019**, *18* (6), 525−529.
(29) Xu, L.; Ramadan, S.; Rosa, B. G.; Zhang, Y.; Yin, T.; Torres, E.; Shaforost, O.; Panagiotopoulos, A.; Li, B.; Kerherve, G.; Kim, D. K.; Mattevi, C.; Jiao, L. R.; Petrov, P. K.; Klein, N. On-Chip Integrated Graphene Aptasensor with Portable Readout for Fast and Label-Free COVID-19 Detection in Virus Transport Medium. *Sensors & Diagnostics* **2022**, *1* (4), 719−730.
(30) Fernández, D. P.; Mulev, Y.; Goodwin, A. R. H.; Sengers, J. M. H. L. A Database for the Static Dielectric Constant of Water and Steam. *J. Phys. Chem. Ref. Data* **1995**, *24* (1), 33−70.
(31) Fernández, D. P.; Goodwin, A. R. H.; Lemmon, E. W.; Levelt Sengers, J. M. H.; Williams, R. C. A Formulation for the Static Permittivity of Water and Steam at Temperatures from 238 to 873 K at Pressures up to 1200 MPa, Including Derivatives and Debye−Hückel Coefficients. *J. Phys. Chem. Ref. Data* **1997**, *26* (4), 1125−1166.
(32) Peyman, A.; Gabriel, C.; Grant, E. H. Complex Permittivity of Sodium Chloride Solutions at Microwave Frequencies. *Bioelectromagnetics* **2007**, *28* (4), 264−274.
(33) Chen, S.; Sun, Y.; Fan, X.; Xu, Y.; Chen, S.; Zhang, X.; Man, B.; Yang, C.; Du, J. Review on Two-Dimensional Material-Based Field-Effect Transistor Biosensors: Accomplishments, Mechanisms, and Perspectives. *J. Nanobiotechnology* **2023**, *21* (1), 144.
(34) Béraud, A.; Sauvage, M.; Bazán, C. M.; Tie, M.; Bencherif, A.; Bouilly, D. Graphene Field-Effect Transistors as Bioanalytical Sensors: Design, Operation and Performance. *Analyst* **2021**, *146* (2), 403−428.
(35) Xia, J.; Chen, F.; Li, J.; Tao, N. Measurement of the Quantum Capacitance of Graphene. *Nat. Nanotechnol* **2009**, *4* (8), 505−509.
(36) Tran, T.-T.; Mulchandani, A. Carbon Nanotubes and Graphene Nano Field-Effect Transistor-Based Biosensors. *TrAC Trends in Analytical Chemistry* **2016**, *79*, 222−232.
(37) Singh, P. S. From Sensors to Systems: CMOS-Integrated Electrochemical Biosensors. *IEEE Access* **2015**, *3*, 249−259.
(38) Garrido-Cardenas, J.; Garcia-Maroto, F.; Alvarez-Bermejo, J.; Manzano-Agugliaro, F. DNA Sequencing Sensors: An Overview. *Sensors* **2017**, *17* (3), 588.
(39) Li, H.; Liu, X.; Li, L.; Mu, X.; Genov, R.; Mason, A. CMOS Electrochemical Instrumentation for Biosensor Microsystems: A Review. *Sensors* **2017**, *17* (12), 74.
(40) Georgakilas, V.; Otyepka, M.; Bourlinos, A. B.; Chandra, V.; Kim, N.; Kemp, K. C.; Hobza, P.; Zboril, R.; Kim, K. S.

Functionalization of Graphene: Covalent and Non-Covalent Approaches, Derivatives and Applications. *Chem. Rev.* **2012**, *112* (11), 6156−6214.

https://doi.org/10.1021/acsaelm.3c00706
ACS Appl. Electron. Mater. 2023, 5, 4925−4932